

Article

Modeling Residual Magnetic Anomalies of Landmines Using UAV-Borne Vector Magnetometer: Flight Simulations and Experimental Validation

Junghan Lee ^{1,2}  and Haengseon Lee ^{2,*}

¹ LIG Nex1 Co., Ltd., Pangyo 13488, Republic of Korea; junghan.lee@lignex1.com

² Department of Electronic Engineering, Sogang University, Seoul 04107, Republic of Korea

* Correspondence: leehs95@sogang.ac.kr; Tel.: +82-2-705-8914; Fax: +82-2-705-8114

Abstract: This study presents an unmanned aerial vehicle (UAV)-borne vector magnetometer (MAG) system and proposes a new data-processing technique for modeling the residual magnetic anomalies of three types of landmines: the metallic antitank M15, the metallic antipersonnel M16, and the minimum-metal antitank M19. The burial depth and magnetic moment of these landmines were estimated using the measured and simulated residual magnetic anomalies based on the proposed UAV-borne vector MAG model. Initial in-flight validation showed a strong correlation between the residual magnetic anomaly maps obtained from measurements and simulations. To verify the detection capability in real-world conditions, the UAV-borne MAG system was tested at the Korean Combat Training Center. Both simulations and experiments demonstrated the effectiveness of the proposed data-processing method and UAV-borne MAG model in accurately modeling the residual magnetic anomalies of landmines with metallic components. This approach will facilitate the automated detection of M15, M16, and M19 landmines with high detection rates and enable accurate classification.



Citation: Lee, J.; Lee, H. Modeling Residual Magnetic Anomalies of Landmines Using UAV-Borne Vector Magnetometer: Flight Simulations and Experimental Validation. *Remote Sens.* **2024**, *16*, 2916. <https://doi.org/10.3390/rs16162916>

Academic Editor: Amin Beiranvand Pour

Received: 23 June 2024

Revised: 6 August 2024

Accepted: 7 August 2024

Published: 9 August 2024



Copyright: © 2024 by the authors. Licensee MDPI, Basel, Switzerland. This article is an open access article distributed under the terms and conditions of the Creative Commons Attribution (CC BY) license (<https://creativecommons.org/licenses/by/4.0/>).

1. Introduction

The need for underground exploration using unmanned aerial vehicles (UAVs) or drones for the purpose of explosive detection at disaster sites is increasing. Land or naval mine detection performed manually by humans is time consuming and the detection location is usually inaccurate, which often results in casualties. Replacing these practices with drones could allow for the safe, rapid, and relatively accurate detection of landmines. If landmine detection drone source technology is developed in line with the 4th industrial revolution, it could eventually be used as a special purpose military drone. Recent studies have explored several detection strategies involving lightweight non-destructive remote sensing sensors mounted on the multi-rotary UAVs for landmine detection, such as ground-penetrating-synthetic aperture radar (GP-SAR) [1,2], fluxgate vector magnetometers (MAGs) [3,4], metal detectors [5,6], and a combination of magnetometer and ground penetrating radar (MAG-GPR) [7]. The benefits of these techniques include accurate autonomous flight capability, the potential for multiple-sensor integration, innovative avionic systems, energy-saving batteries, and significant reductions in costs and maintenance operation requirements.

UAV-borne GPR is a primary system used for UAV-based landmine detection. However, estimating its relative permittivity requires knowledge of the burial depth, such as in experimental scenarios, and GPR measurement ranges. This limitation means that the depths of undiscovered buried landmines cannot be accurately determined in moist surface layers or shallow-water environments because radar signals are significantly affected by

the dielectric properties of the materials. Therefore, a single GPR sensor cannot detect all landmines in various environments.

To address this issue, various sensing principles and methods for UAV-borne GPR and UAV-borne MAG sensor fusion have been tested in army field exercises for mine countermeasure and explosive hazard defeat missions [8,9]. The UAV-borne MAG system detects landmines by measuring the magnetic anomalies caused by buried targets magnetized by the Earth's magnetic field. Since these magnetic anomalies are not significantly affected by soil permittivity, the MAG system can assist the GPR system in detecting landmines.

The first step in a landmine exploration is to survey a large area quickly with a UAV-borne MAG. The location, burial depth, and type of landmine are identified, without information on the dielectric constant of the land in the exploration area. A precise exploration may then be performed using UAV-borne GPR, based on the preliminary information provided by the UAV-borne MAG. With this approach, landmine exploration efficiency is improved.

A UAV-borne GPR survey involves active detection, in which electromagnetic waves are emitted and received, whereas a UAV-borne MAG survey is passive and is based on received magnetic fields. Each of these approaches has benefits and drawbacks due to their inherent limitations under various flight conditions, and neither provides optimal detection performance on its own.

A MAG sensing technique for UAV-based landmine detection, developed from flight parameter simulations and the data obtained in experiments, can compensate for the limitations of UAV-borne GPR sensing. The main obstacles in UAV-borne MAG sensing are:

- It is difficult to minimize and compensate for the magnetic interference noise generated by the UAV. Multi-rotor UAVs are usually small in size, with densely distributed components containing ferromagnetic materials, such as brushless motors, which form magnetic dipoles. Studies on the electromagnetic characteristics of the interference by multi-rotor UAVs have been conducted [10–14]. The primary magnetic interference from UAVs occurs when current flows through aerial electronic equipment, including servo and motor systems, as well as DC battery cables. Unwanted magnetic-field contributions from the UAV can be reduced by suspending the magnetic sensor payload below the rotary UAV platform such that it is physically separated from it. However, the technical realization of this separation leads to additional challenges related to MAG attitude variations during flight. To increase the probability of detecting landmines, the magnetic sensor should generally be placed close to the ground. Additionally, the length of the suspended cable with the magnetic sensor must be increased and the UAV's flight altitude must be lowered to detect the magnetic anomaly of landmines. Multi-rotor UAVs are subject to a ground effect when operating in close proximity to rigid surfaces, which impacts the UAV's attitude performance during the flight [15]. The swing of the suspended MAG and the attitude variation in a multi-rotor UAV increase flight instability, directional position errors, and the effect of ground vibrations, ultimately degrading the quality of the magnetic data [16]. Consequently, in practice, the MAG used for landmine detection cannot be suspended and must be fixed to the drone's body. Compensation methods [17–20] have been proposed to separate the magnetic interference generated by UAVs from the outputs of the vector MAG, thereby improving the quality of aeromagnetic data. However, these approaches require an additional compensation flight for each UAV change, with the compensation and validation flights conducted under the same flight conditions and ideal stable magnetic field environments.
- Magnetic anomaly detection (MAD) using vector MAGs mounted on drones with changing attitude is complex. This is because the outputs of the vector MAGs consist of three components of the magnetic field vector, and all of them are sensitive to both the attitude of the magnetic sensor and the maneuver of the drone. There has been little research on the magnetic compensation to improve the quality of data measured by the vector MAGs fixed on a multi-rotor UAV [21,22]. However, the compensation

parameters were estimated without accounting for changes in MAG's attitude. As a result, there is no compensation for the actual motion changes of the drone. To date, progress has been made in improving the quality of magnetic data collected by UAVs using the horizontal [23] or vertical [24] gradient vector MAGs. However, these methods require a specialized payload configuration with multiple magnetic sensors and involve complex procedures for extracting compensation parameters. Developing a straightforward and robust method to handle attitude variation in the vector MAG caused by the UAV's motion remains a significant challenge. A new MAD technique is needed to obtain reliable magnetic field data despite changes in the UAV's motion, without requiring additional compensation flights and complex procedures.

In this paper, we present a UAV-borne vector MAG model that accounts for variations in the UAV's flight attitude and propose a new data-processing technique for modeling the residual magnetic anomaly of landmines using UAV-acquired MAG data. To the best of our knowledge, the proposed UAV-borne vector MAG model is a novel approach to landmine detection that has not been previously examined. Our focus is on the flight simulations and experimental verification of the UAV-borne MAG system as well as on efficient and automated data-processing and interpretation methods.

The remainder of this paper is organized as follows: Section 2 details the newly developed UAV-borne MAG measurement system and the proposed data-processing method. Section 3 presents the flight simulation and experimental results, focusing on modeling residual magnetic anomalies in the metallic antitank M15, metallic antipersonnel M16, and minimum-metal antitank M19 landmines. Section 4 provides a discussion of the findings, and Section 5 offers the conclusions of the study.

2. Materials and Methods

2.1. UAV-Borne MAG Measurement System

MAG data were collected using a newly developed UAV-borne MAG measurement system (Figure 1) based on the architecture described in [7]. The main components are:

- A flight control subsystem composed of a UAV flight controller (model Pixhawk2 Cube Orange) and common positioning sensors on board the UAV. These sensors consist of an inertial measurement unit, a barometer, and a conventional Global Navigation Satellite System (GNSS) receiver. To minimize the heading error of the UAV, a magnetic compass sensor is installed on top of it.
- An accurate positioning subsystem that provides centimeter-level accuracy. It includes a laser altimeter (model SF11c; Lightware) [25] and a multi-band real-time kinematic (RTK)-GNSS (model C-RTK 9Ps; CUAV) [26]. The latter consists of an RTK antenna and an RTK receiver. RTK corrections are received from a GNSS-based ground station and sent to the RTK receiver. This set-up achieves a position accuracy of $1\text{ cm} \pm 1\text{ ppm}$. A multi-band RTK was selected because it offers superior accuracy and availability (i.e., the percentage of time that corrected coordinates are provided), greater robustness (such as when operating in areas with limited sky view), and faster deployment times than a single-band RTK, as demonstrated in the previous study [4]. The multi-band RTK supports GPS L1C/A, L2C; GLONASS L1OF, L2OF; Galileo E1B/C, E5B; and BeiDou B1I, B2I.
- A MAG subsystem consisting of a lightweight (85 g), compact fluxgate vector MAG (model 1540; Applied Physics Systems) [27] installed at the center of the UAV, ~30 cm below the UAV's center, to minimize the magnetic noise interference of the UAV. The MAG's attitude (roll, pitch, and yaw) is estimated from the MAG's measurements [28–30]. The MAG and the laser altimeter are mounted at the same vertical position on the UAV through a rigid rod, so that the MAG's altitude is consistent with the altitude of the UAV during the UAV flight.
- A companion single computer (model LattePanda 3 delta; LattePanda) [31] that receives the MAG measurements and transmits the data to the ground station through a 5.0 GHz wireless data link modem.

- A ground station consisting of two conventional laptops: one receives the MAG measurements and the positioning and geo-referring information and the other monitors the UAV flight status using ground control station software (Mission Planner version 1.3.79). Geo-referred measurements are processed using the MAG data-processing methodology described in Section 2.2 to detect the magnetic anomaly of a landmine buried underground.
- The communication subsystem has a receiver at 2.4 GHz (model MK15; SIYI) [32] that is linked with the pilot remote controller and a wireless transceiver at 5.0 GHz (model pMDDL5824; Microhard) [33] to allow the ground station to receive and monitor the MAG measurement data in real time. The two frequencies were selected to minimize any potential electromagnetic interference between controlling the UAV flight and receiving the MAG data.

With the newly developed UAV (Figure 2), a payload of up to 4 kg weight can be mounted, thus providing capacity for further improvements of the prototype, such as additional detecting sensors or devices (e.g., ground-penetrating radar, as in our previous study [7]). The total weight of the payload, consisting of the main systems and subsystems described above, is approximately 1 kg (excluding batteries). With a payload of 1 to 2 kg, the UAV can hover for around 70 min, which is sufficient for experimental validation of landmine detection tests. Detailed specifications of the newly developed UAV-borne MAG system are provided in Table 1.

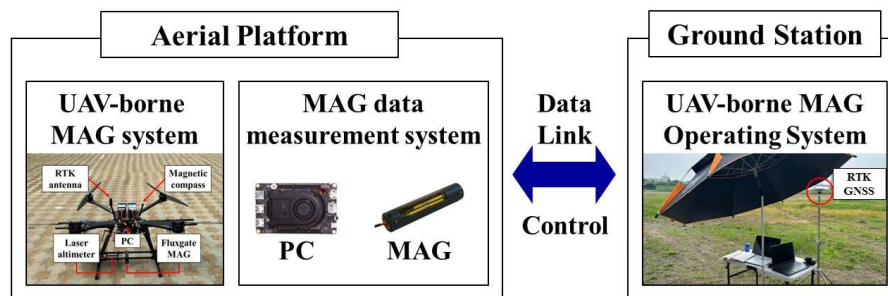


Figure 1. Configuration of the unmanned aerial vehicle (UAV)-borne magnetometer (MAG) measurement system; aerial platform and ground station.

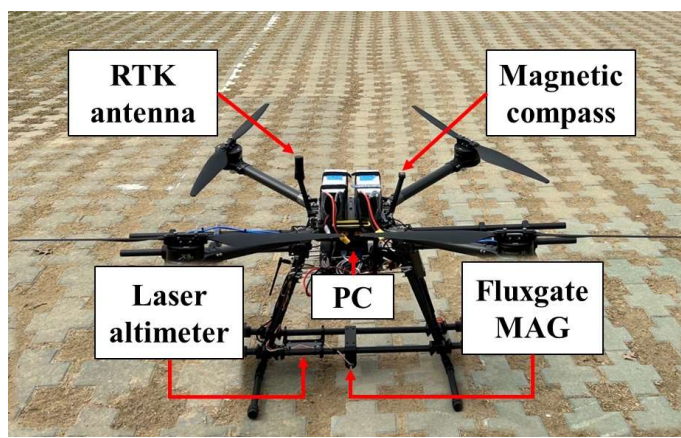


Figure 2. Photograph of newly developed UAV-borne MAG system.

Table 1. Specifications of the newly developed UAV-borne MAG system.

Parameters	UAV	MAG
	Specifications	Parameters
		Specifications
Multi-copter type	Quad	Measurement range
Size	920 (D) × 920 (W) × 700 (H) mm	Size
Total weight	12.9 kg (including batteries)	Resolution
Maximum takeoff weight	24.9 kg	Accuracy
Battery	LiPo (6S 30,000 mAh) 2pcs	Axis alignment
Maximum flight speed	10 m/s	Noise level
Hovering endurance	70 min (@payload 2 kg)	Weight
		$\pm 6.5 \times 10^4$ nT
		25 (Diameter) × 122 (L) mm
		0.03 nT
		$\pm 0.5\%$ full-scale
		Better than $\pm 0.2^\circ$
		± 0.5 nT
		85 g

Since the motors, located diagonally from the center of the drone, rotate in opposite directions, if all of them have the same revolutions per minute (RPM), the total magnetic interference field at the center of the drone is theoretically zero. However, when the multi-rotor UAV is in flight, the RPM of the motors vary, resulting in a non-zero total magnetic interference field from the UAV that is inversely proportional to the cube of the distance from the center [3]. In the absence of electromagnetic interference (EMI) reduction techniques, a quad-rotor drone without landing gear servos produces lower levels of magnetic interference than a hexa-rotor drone with landing gear servos, because it has fewer motors [14]. In this study, the magnetic interference measured 30 cm away from the center of the quad-rotor drone was <5 nT. A quad-rotor drone is therefore the best choice for geomagnetic surveying. The high-frequency magnetic noise can be separated from the UAV's acquired magnetic data using the data-processing methods described in Section 2.2.

Our newly developed UAV-borne MAG system adopts the EMI reduction techniques, such as twisting the DC cables and demagnetizing the steel components. In the absence of landing gear servos or an increase in the distance between the motors and the intended MAG installation point, the interference magnetic noise from the quad-rotor drone can be minimized. This approach is also the fundamental starting point for the success of the data-processing method presented below.

2.2. UAV-Borne MAG Data-Processing Methodology

A flowchart of the proposed method for estimating the burial depth and magnetic moment of M15, M16, and M19 landmines from UAV-borne MAG data is shown in Figure 3, which includes MAG data processing and an analytical interpretation of the results.

The input of the process is the UAV-borne MAG data acquired from the fluxgate-vector MAG fixed to the UAV and the MAG's positioning information (latitude, longitude, and height) as determined from UAV's RTK-GNSS system and a laser altimeter. The MAG's attitude (roll, pitch, yaw) is calculated from the MAG's raw data [28–30].

The UAV-borne MAG's raw data consist of three components:

- Magnetic field interference caused by the UAV's high frequency noise.
- The regional geomagnetic field (trend).
- The residual magnetic anomaly, as described in the magnetic anomaly modeling (Section 2.3).

To estimate the burial depth and magnetic moment of a landmines, the UAV-borne MAG data are processed as follows:

- Low-pass filtering: the high-frequency noise caused by the UAV can be removed by low-pass filtering. The cutoff frequency of the low-pass filter must be selected based on the frequency characteristics of the target signal. Generally, the frequency of the noise generated from a drone's motor is proportional to the rotation speed of the motor. This frequency is linearly proportional to the UAV's speed (v) but inversely proportional to the distance (r) from the target to the MAG ($f = 0.85v/r$) [34].
- Detrending: to effectively detect the residual magnetic anomalies of M15, M16, and M19 landmines, a detrending method was used to eliminate the regional trend of the

geomagnetic field. This method fits a linear plane to the data, removing the regional trend across the entire map.

- Estimation of burial depth: a portion of the residual magnetic anomaly curve is extracted to estimate the burial depth of a landmine using the full width at half height (FWHH) method with reduction to the pole (RTP) [35]. The altitude of the UAV, measured by the high-precision laser altimeter, is then subtracted from the extracted FWHH. Although this is an old technique, it is robust for compact targets relative to their depth or distance. For a magnetic dipole sphere, the distance from the MAG to the landmine is approximately equal to the half width of the residual anomaly at half its peak amplitude. The landmine is located at the point where the center of the residual anomaly peak is at its maximum.
- Analytical interpretation: the burial depth and magnetic moment of landmines are estimated using the UAV-borne MAG model, which accounts for variations in the UAV's flight attitude (see Section 2.3).

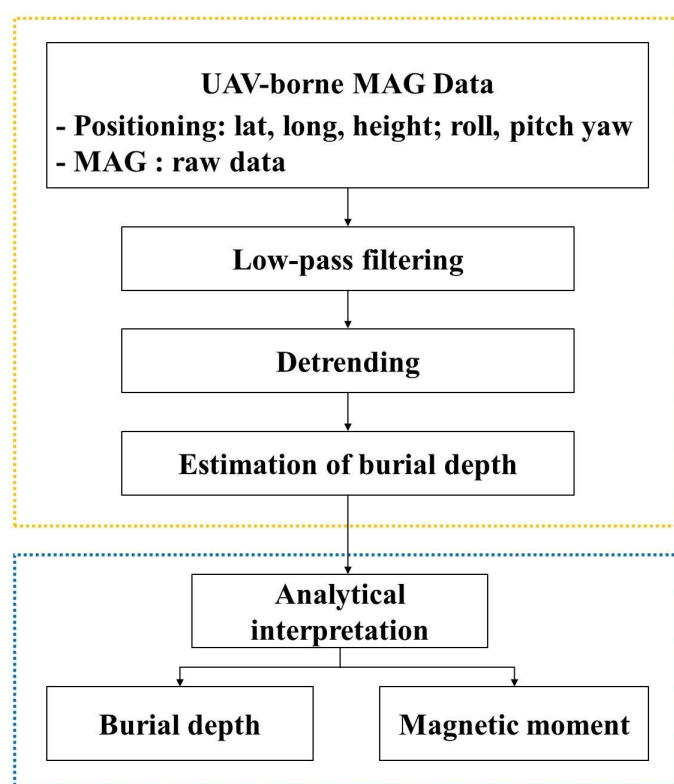


Figure 3. Flowchart of the proposed method for processing UAV-derived MAG data to estimate the burial depth and magnetic moment of M15, M16, and M19 landmines. The dotted yellow box and dotted blue box indicate the MAG data-processing results and an analytical interpretation of the results, respectively.

2.3. A UAV-Borne MAG Model That Accounts for Variations in the UAV's Flight Attitude

The magnetic field of ferromagnetic landmines can be approximated using a magnetic dipole model when the distance from the target to the MAG's measurement position is at least three times greater than the target's dimension, a condition satisfied in this study.

A magnetic dipole located at $\mathbf{r}_0 = (r_{0x}, r_{0y}, r_{0z})$ with a magnetic moment $\mathbf{m} = (m_x, m_y, m_z)$ generates a magnetic field $\mathbf{B}_{dipole} = (B_{ox}, B_{oy}, B_{oz})$ at the observation point \mathbf{r}_p as referenced in [36]:

$$\mathbf{B}_{dipole}(\mathbf{r}, \mathbf{m}) = \frac{\mu_0}{4\pi} \left[\frac{3(\mathbf{m} \cdot \mathbf{r})\mathbf{r}}{r^5} - \frac{\mathbf{m}}{r^3} \right] \quad (1)$$

where μ_0 is the permeability of free space, equal to $4\pi \times 10^{-7}$ H/m, \mathbf{r} is the distance vector from the observation point \mathbf{r}_p to the dipole \mathbf{r}_0 , and r is its modulus.

The dipole model in electromagnetism disregards the direction of the Earth's magnetic field and considers only six parameters: a three-dimensional position vector and a three-dimensional magnetic moment vector. However, the magnetic anomalies of landmines result from the combined effects of induced magnetization in the current geomagnetic field and remanent magnetization. In this paper, we assume the remanent component is negligible, focusing on the magnetic anomaly caused primarily by the induced component, which aligns parallel to the Earth's magnetic field [37].

A ferromagnetic landmine becomes magnetized in the direction of the Earth's magnetic field, based on local inclination and declination. This magnetization generates an induced magnetic field that disrupts the Earth's magnetic field in the surrounding area, creating a magnetic anomaly signal.

Figure 4 shows the reference and body coordinates for variations in the UAV's flight attitude. First, we describe Equation (2), which models the residual magnetic anomaly of a landmine without considering changes in the MAG's attitude in the reference coordinate system. Based on this, we propose Equation (3), which includes the MAG's attitude changes with respect to the body coordinate system.

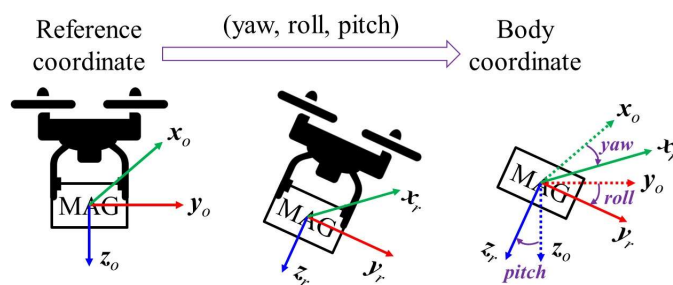


Figure 4. Reference and body coordinates for the variations in the UAV's flight attitude.

The total magnitude of the residual magnetic anomaly of a landmine (B_o) is the superposition of the x-, y-, and z-components (B_{ox} , B_{oy} , and B_{oz}) of the dipole's magnetic field (\mathbf{B}_{dipole}), considering the inclination and declination of the geomagnetic field, as shown in Equation (2). This total magnitude can be expressed using sine and cosine functions and the summation of these components. The reference Cartesian coordinate system for Equation (2) aligns with the three axes of the vector MAG, as shown in Figure 5. When the UAV is in flight, the MAG's attitude constantly changes, causing the output of the vector MAG to vary with respect to the body coordinates. Consequently, Equation (2) can be modified to account for the MAG's attitude changes with respect to the body coordinates, as shown in Equation (3).

$$B_o = \{B_{ox}\cos(d)\cos(i)\} + \{B_{oy}\sin(d)\cos(i)\} + \{B_{oz}\sin(i)\} \quad (2)$$

$$\begin{aligned} B_r = & \{B_{ox}\cos(d - \text{yaw})\cos(i - \text{roll} - \text{pitch})\} \\ & + \{B_{oy}\sin(d - \text{yaw})\cos(i - \text{roll} - \text{pitch})\} \\ & + \{B_{oz}\sin(i - \text{roll} - \text{pitch})\} \end{aligned} \quad (3)$$

where d is the degree of declination, i is the degree of inclination, and yaw, roll, and pitch are the MAG's attitudes.

Finally, the landmine burial depth and magnetic moment are estimated from Equation (3) based on the MAG data are processed in Section 2.2.

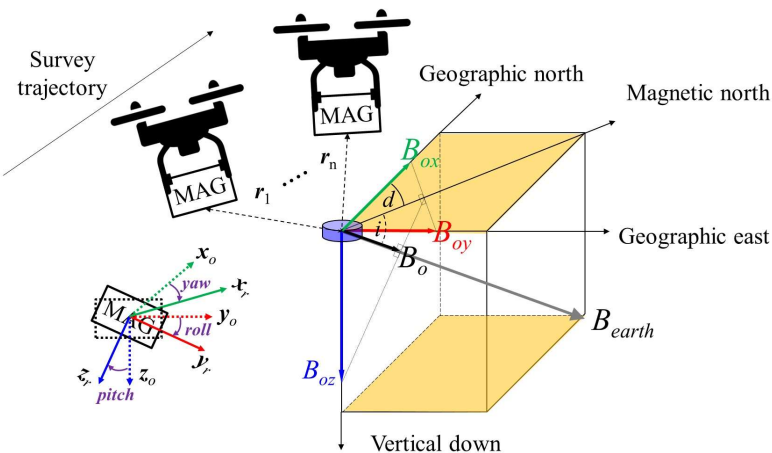


Figure 5. The UAV-borne MAG model that accounts for variations in the UAV's flight attitude and the measurement scheme.

3. Results

Figure 6 shows a schematic diagram of the UAV-borne MAG's flight simulation and experiment, where the burial depth and magnetic moment of detected landmines are estimated. The UAV system traveled uniformly at 1 m/s and an altitude of 1 m across the surface, collecting magnetic anomaly data from buried M15, M16, and M19 landmines along a survey line positioned directly above the landmines and oriented perpendicular to their vertical axis. The landmines were buried at a depth of 10 cm at specified locations, and MAG measurements were repeatedly taken for each landmine type. Both the MAG and GNSS systems had a sampling rate of 10 Hz. Since the experiment was conducted in the northern hemisphere, the residual magnetic anomaly curves of the landmines exhibited negative-positive behavior along the survey direction. To correct for the asymmetry of these residual anomalies, we applied the RTP method to make them symmetric.

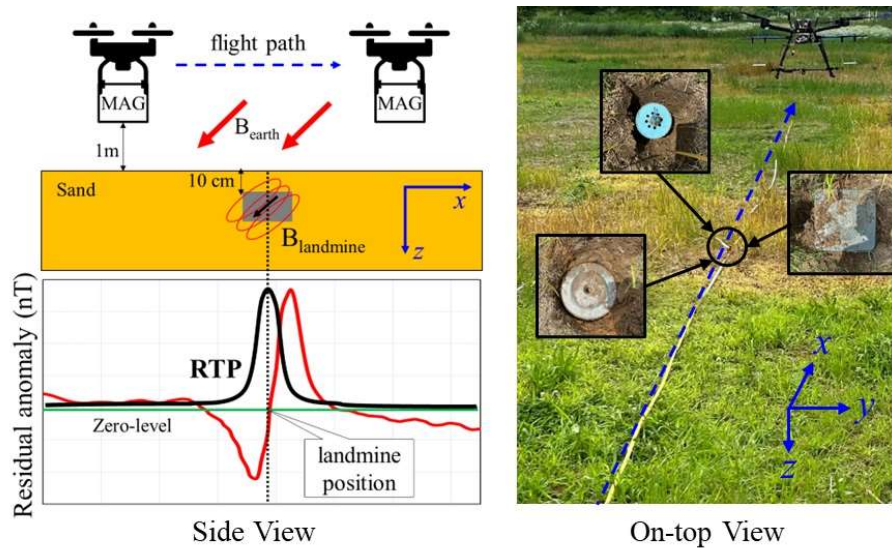


Figure 6. Schematic diagram of the UAV-borne MAG data acquisition experiment.

3.1. MAG Data Processing

The collected MAG raw data included high-frequency noise from the UAV, the regional geomagnetic field (trend), and the residual landmine anomaly signals. To eliminate the high-frequency noise, a low-pass filter with a cut-off frequency of 0.8 Hz was used. Removing the trend components allowed for the extraction of the residual magnetic anomalies, which are shown as solid black lines in Figure 7a.

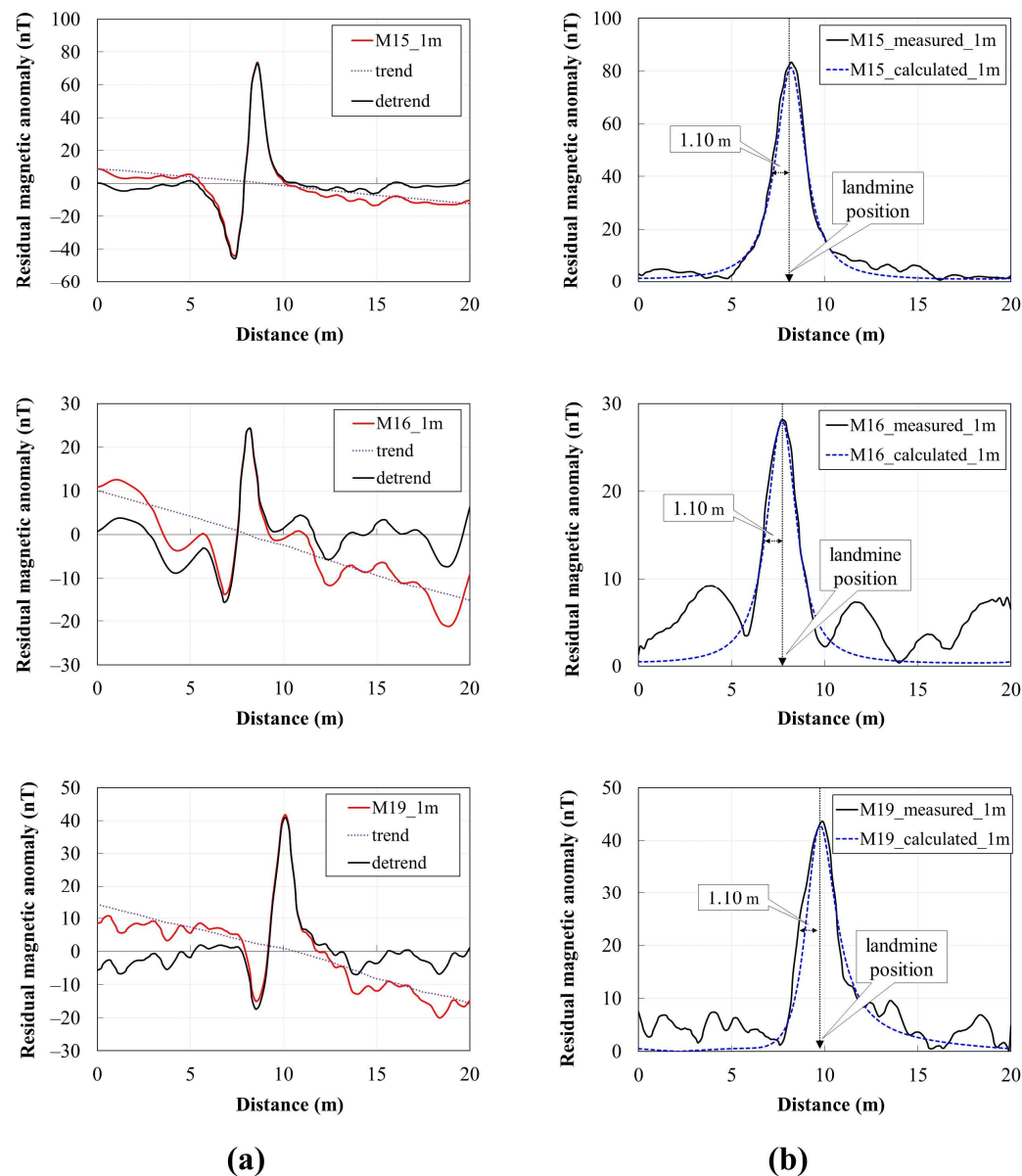


Figure 7. Residual magnetic anomalies: **(a)** using the detrending method (solid black lines) and **(b)** using the RTP method, with measured anomalies shown in solid black lines and calculated anomalies shown in dotted blue lines.

Figure 7b shows the symmetric residual magnetic anomalies obtained using the RTP method. The measured residual anomalies are represented by solid black lines, while the anomalies calculated from the model are shown as dotted blue lines. The peak residual anomaly amplitudes of the landmines decreased in the following order: M15 > M19 > M16. The extracted FWHH after RTP was 1.1 m. The estimated burial depths of the landmines matched their actual burial depths.

3.2. Analytical Interpretation

The structure and metallic composition of the M15, M16, and M19 landmines, as described in the US Army reference [38], are outlined as follows:

- The M15 landmine features a large, circular steel body with a diameter of 33 cm and a height of 15 cm. It includes a central metal pressure plate as part of its fuze mechanism. The primary metallic components are the body and pressure plate, though additional metal parts may be present in the fuze and explosive assembly.

- The M16 landmine has a cast iron body encased in a thin steel sleeve, with a diameter of about 10 cm and a height of 20 cm. The core structure is cast iron, providing strength and weight, while the steel sleeve offers additional protection. Key metallic parts include the body, sleeve, and pressure plate, along with other internal metal components related to the fuze and explosive mechanism.
- The M19 landmine has a large, square plastic body measuring 33 cm in diameter and 10 cm in height. It contains only a few metal components: a thin stainless steel pressure plate, a copper detonator capsule, and a stainless steel firing pin, all embedded within the plastic body. Despite its substantial plastic casing, the M19 is notable for its minimal metal content.

Based on the provided information, the magnetic moments of the landmines were estimated using Equation (3), with parameter values detailed in Table 2. These estimates were used to calculate the residual magnetic anomalies (dotted blue lines) for the M15, M16, and M19 landmines, which closely matched the measured residual anomalies (solid black lines in Figure 7b). The agreement between the measured and calculated residual magnetic anomaly curves for the M15, M16, and M19 landmines is illustrated in Figure 7b. The magnetic moments of the landmines were ranked as follows: M15 > M19 > M16. Consequently, the peak residual anomaly of the M19 landmine was higher than that of the M16 landmine. These distinctive magnetic properties highlight the differences between the minimal-metal M19 and the metallic M16 landmines.

Table 2. Estimated parameters for the analytical interpretation.

Parameter Name	Estimated Value		
	M15	M16	M19
Magnetic moment (Am^2)	(0.522, -0.904, 0.930)	(0.130, -0.225, 0.231)	(-0.326, 0.087, -0.338)

3.3. In-Flight Validation of Landmine Anomaly Detection with Varying Flight Parameters

3.3.1. First Validation Scenario

The set-up of the first validation scenario for the UAV-borne MAG measurement is shown in Figure 8. The size of the survey area was 2×14 m. The UAV traversed the surface along five survey lines (numbered #1 to #5), starting from point A (37.5748148°N , $126.6697209^\circ\text{E}$) and ending at point B (37.5748659°N , $126.6695758^\circ\text{E}$). The landmines were buried at designated locations, concealed beneath sand at a depth of 10 cm. The flight speed was 1 m/s at an altitude of 0.5 m, the survey lines were spaced 0.5 m apart, and the sampling distance intervals of the RTK position and the MAG were 10 cm for the MAG data analysis.

In the test, the UAV's heading was fixed at a constant value, aligned with the desired main course over the ground. The UAV system moved along each survey line without changing its heading to collect the MAG data. A heading of -79.5° to -63.0° was maintained toward the magnetic north direction, considering a magnetic declination of -8.8976° to -8.8933° and an inclination of 54.6050° to 54.6062° based on the International Geomagnetic Reference Field (IGRF) [39].

In measurements taken with UAVs, obtaining uniform geo-referenced magnetic measurement data acquisitions is very difficult because the UAV deviates from the ideal flight path due to wind conditions and positioning system uncertainties. Achieving positional accuracy within a few centimeters during flight requires tens of hours of RTK position reception at the ground station beforehand. However, in field experiments, we set the positional accuracy to 30 cm, which was achieved in approximately 1 to 2 h. Furthermore, during experimental flights, it was observed that when the UAV changed direction, its speed usually decreased, resulting in oversampling.

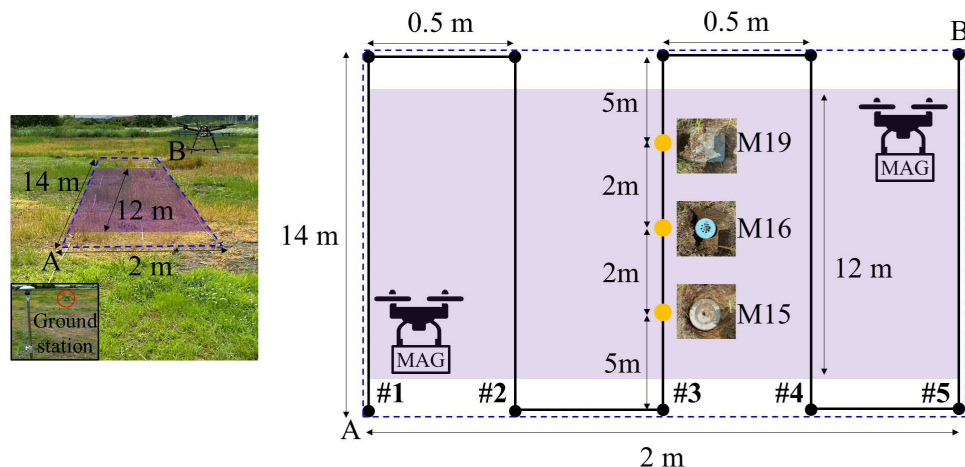


Figure 8. Schematic diagram of the first in-flight validation site. The UAV surveyed five lines (numbered #1 to #5), starting at point A and ending at point B.

To ensure the quality of MAG data processing, only data acquired at points where the flight speed was maintained at 1 m/s in each survey line were post-processed. The purple box in Figure 8 represents the region (size 2×12 m) containing the post-processed data at the survey lines. Figure 9 shows the measured total magnetic intensity map in the Universal Transverse Mercator (UTM) coordinate system. In the analysis of the MAG measurement data, the original flight path oriented in a northwest direction was not rotated and aligned along the UTM x-y axis because the MAG's yaw must be considered for the UAV-borne MAG model. The variations in the roll, pitch, and yaw of the MAG sensor during flight are depicted in Figure 10. The standard deviations of the roll, pitch, and yaw were 0.4° , 0.5° , and 0.9° , respectively.

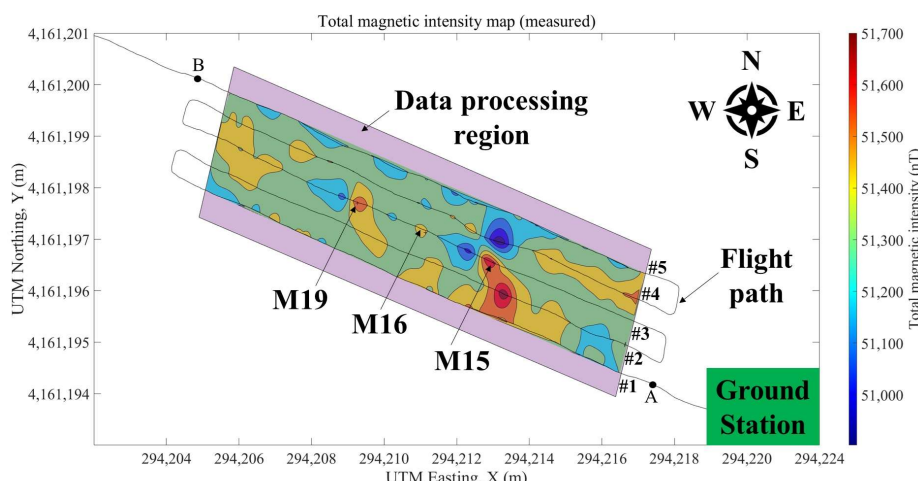


Figure 9. Measured residual magnetic anomaly map from the UAV survey. The UAV surveyed five lines (numbered #1 to #5), oriented in a northwest direction, starting at point A and ending at point B.

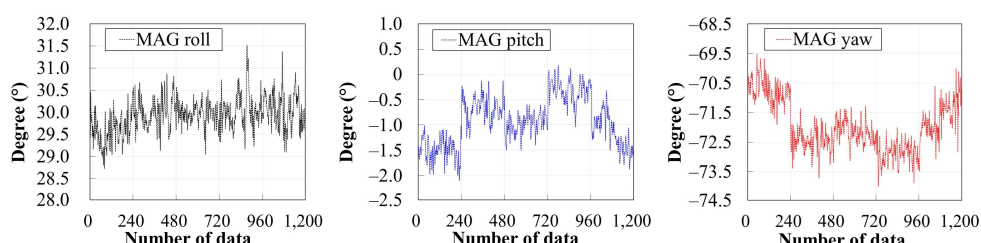


Figure 10. MAG's attitude variation during the flight.

Figure 11 shows the measured and simulated residual magnetic anomaly map of the pre-processed MAG data for the region shown in Figure 9. The simulated map, generated using Equation (3), reflects the MAG's flight attitude along the five survey lines (dotted black lines).

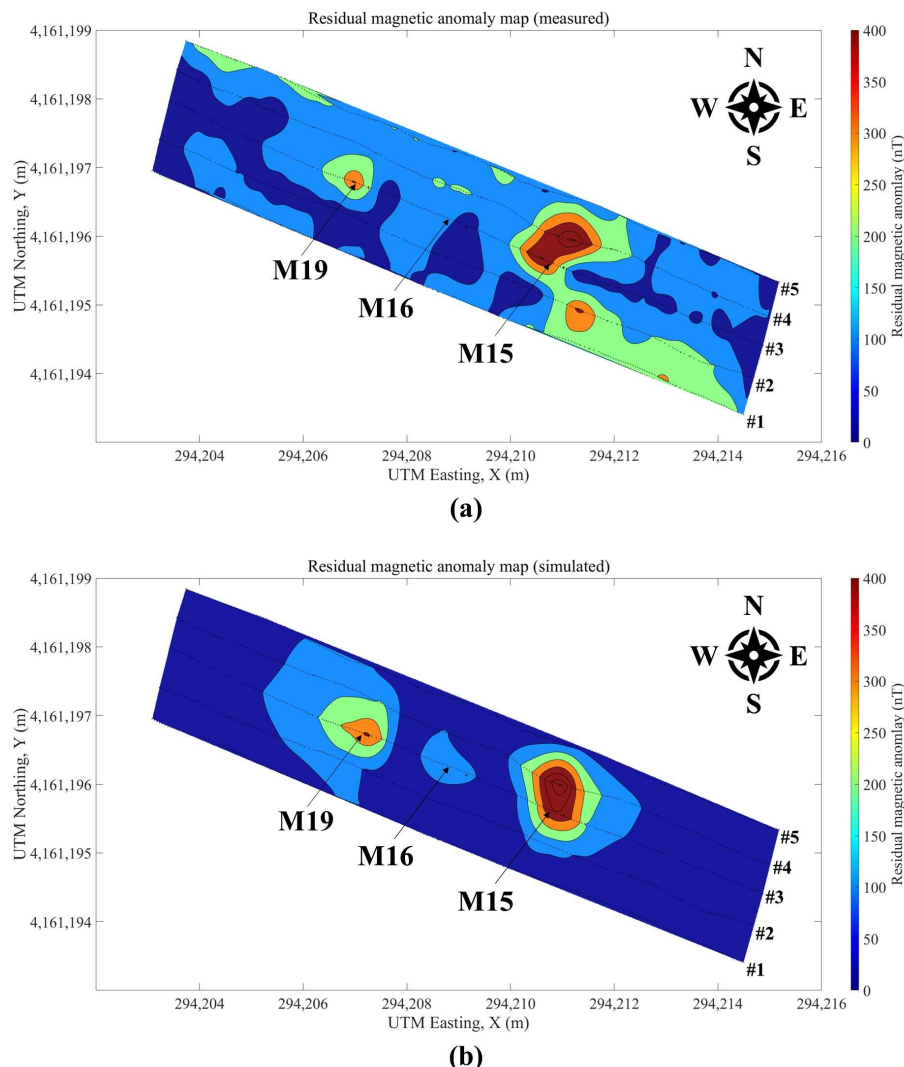


Figure 11. Comparison of the measured (a) and simulated (b) 2D maps of the residual magnetic anomaly. The UAV surveyed five lines (numbered #1 to #5), oriented in a northwest direction.

The residual magnetic anomalies from the M16 landmine were not clearly visible on the map. Figure 12 shows the residual magnetic anomalies detected along survey line #3. The anomalies related to M16 are relatively small compared to those of M15 and M19 landmines and are only slightly larger than the surrounding background residual magnetic anomaly. Given that the positional accuracy for this experiment was set to 30 cm, the difference between the measured values and the positions of the landmines detected in the simulation was approximately 30 cm.

Despite the presence of small, unrelated anomalies that caused discrepancies between the measured and simulated residual magnetic anomaly maps in Figure 11, the detected positions and residual magnetic anomaly characteristics of the M15, M16, and M19 landmines generally aligned well between the measured and simulated results. The detected residual magnetic anomalies were consistent with the experiment's positional accuracy. These results demonstrate the effectiveness of the data-processing and modeling methods presented in this paper.

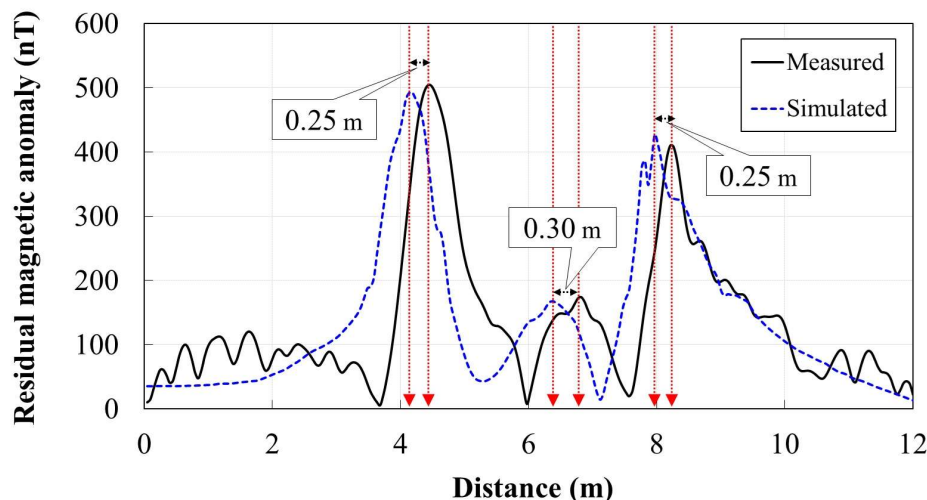


Figure 12. Comparison of the measured (solid black lines) and simulated (dotted blue lines) 1D residual magnetic anomaly signal along the survey line #3.

3.3.2. Second Validation Scenario

The UAV-borne MAG system for landmine detection was then validated at the Korea Combat Training Center (KCTC), located in Inje County, Gangwon Province (Figure 13). The size of the survey area was 40×60 m. Members of the Republic of Korea Army manually buried various types of metallic landmines at positions unknown to the authors in a verification experiment aimed at the detection of unknown metallic landmines using a UAV-borne MAG measurement system. The landmines were arranged vertically in six rows (numbered #1 to #6) on a grid map, extending from point A to point B. A total of 43 metallic landmines (M15, M16, POMZ) were targeted for detection: ten M15 landmines in row #1 and nine in row #2; six M16 landmines in row #3 and six in row #5; and six POMZ landmines in row #4 and six in row #6. The landmines were laid with a vertical spacing of ~ 10 m and a horizontal spacing of ~ 5 m.

The POMZ landmine features a cylindrical or slightly domed metal casing, typically made of steel or cast iron. It has a diameter of 6 cm and a height of 13 cm. The internal components, including the pressure plate and firing pin, are made from high-strength metal alloys [38].

The flight speed was 1 m/s at an altitude of 0.5 m, with a survey line spacing of 0.5 m and a sampling distance interval between the RTK position and the MAG of 10 cm. The UAV surveyed eighty lines, oriented in a southeast direction, starting at point A and ending at point B. During the survey, the UAV's heading was fixed in the southeast direction, aligned with the desired main course of the survey lines. The entire survey, which was completed in two separate flights, took a total of 80 min. Figure 14 shows the measurement results, including (a) the total magnetic intensity map and (b) the residual magnetic anomaly map. Since the burial depth and location of the landmines were unknown to the authors, the actual locations of the manually buried landmines (Figure 13) may have differed from the locations detected by the UAV-borne MAG. Therefore, in this paper, the detection probability was estimated based on the location of the anomaly rows within the array and the number of anomalies in each row (indicated by the solid black box), as shown in Figure 14.

When merging the maps from the separate flights, irregularities emerged due to inconsistencies in the geo-referenced measurement data, resulting in artifacts such as straight lines appearing on the maps shown in Figure 14b. Additionally, residual anomalies not caused by landmines were detected outside the landmine array (indicated by the dashed black box). However, these artifacts and additional anomalies do not affect the detection of the M15, M16, and POMZ landmines. The flight altitude of less than 1 m

ensured a 100% detection rate for the M15, M16, and POMZ landmines. These results experimentally validated the flight conditions discussed in this paper.

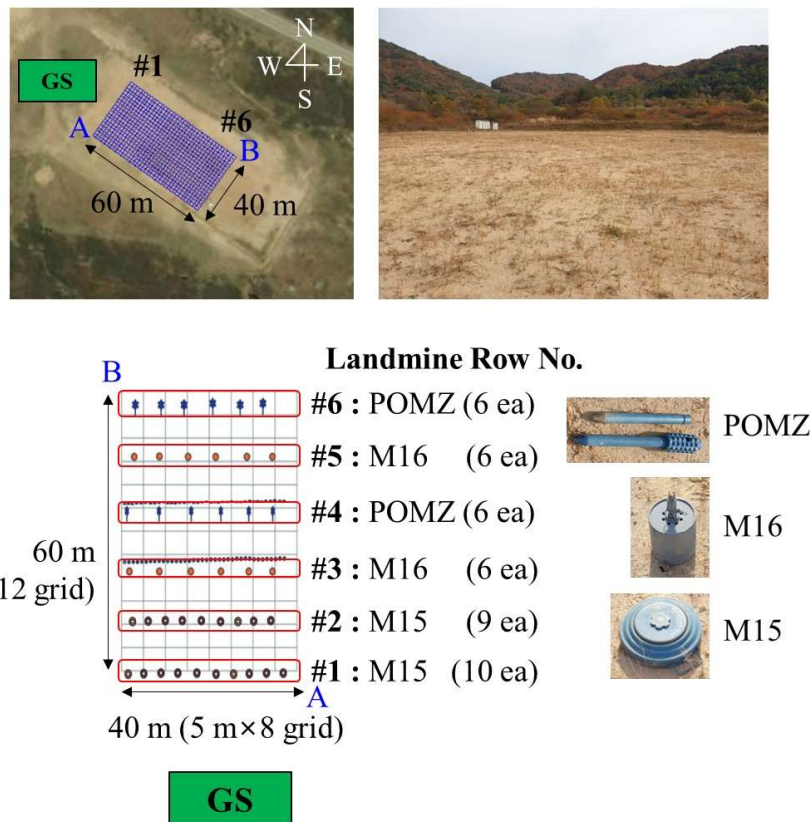


Figure 13. Schematic of the buried landmines and the second scenario in-flight validation site. The landmines were arranged vertically in six rows (numbered #1 to #6) on a grid map, extending from point A to point B.

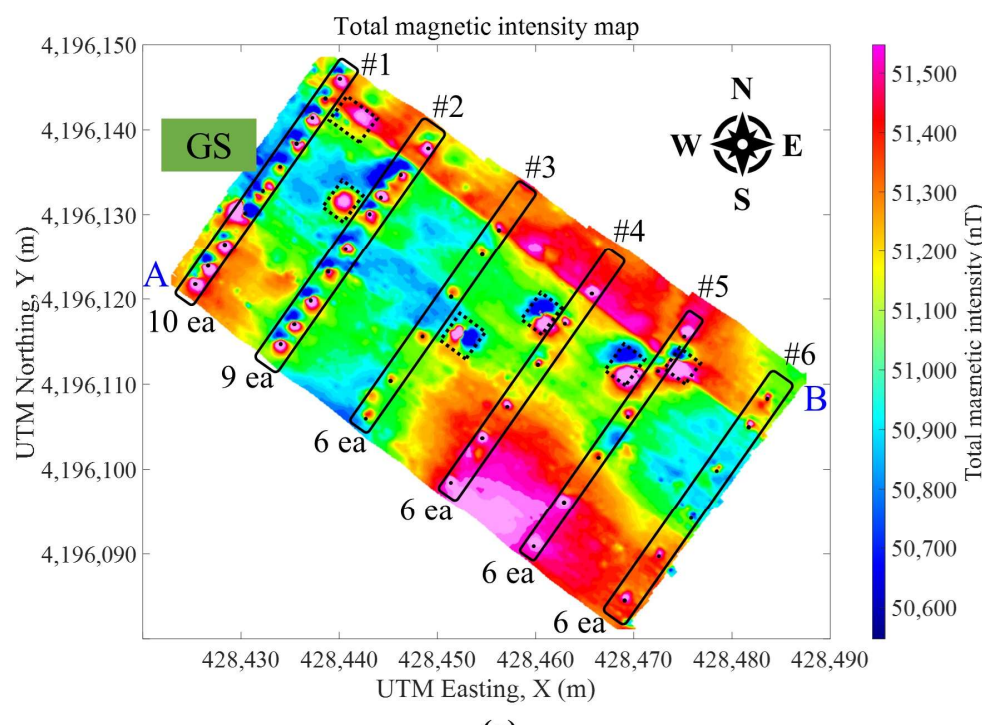


Figure 14. Cont.

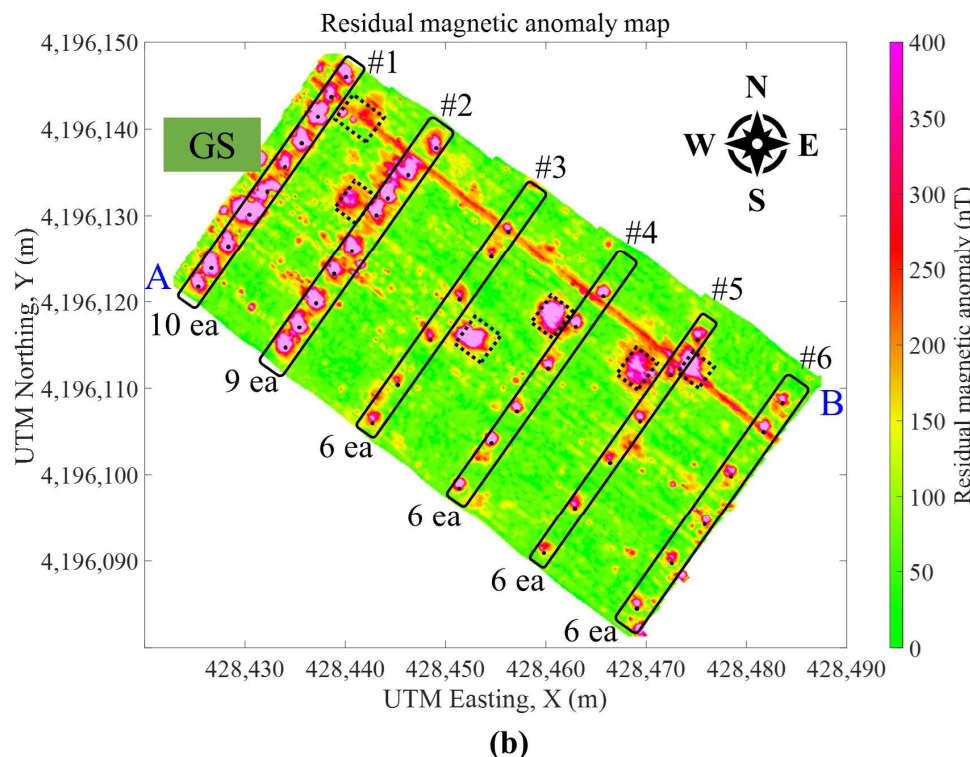


Figure 14. (a) Total magnetic intensity map and (b) residual magnetic anomaly map from the second in-flight verification. The UAV detected landmines in six rows (numbered #1 to #6) on the map, oriented in a southeast direction, starting at point A and ending at point B.

4. Discussion

The simulation and experimental results showed that M15, M16, and M19 landmines can be detected using our UAV-borne MAG system, based on the magnetic dipole model and considering variations in flight parameters. The proposed method accurately estimated the burial depth and magnetic moment of the landmines and successfully classified them under flight conditions, despite positional uncertainties. The improvements and differences between the present study and previous studies are discussed below.

Previous experimental studies using UAV-borne MAG systems only identified magnetic anomaly locations using the analytical method [3] or moving average technique [4], without addressing landmine depth or classification. This study introduces a UAV-borne MAG model that enhances the quality of magnetic data by accounting for the MAG's attitude. This enhancement allows for the detection of small anomalies related to M15, M16, and M19 landmines under various flight conditions. Additionally, the present study estimates the burial depth and magnetic moment of these landmines by modeling the residual magnetic anomaly using the UAV-borne vector MAG model.

Compared with the previous compensation methods [23,24] using the UAV-borne horizontal or vertical gradient vector MAG, the proposed method in this study offers significant advantages in simplicity and robustness. It eliminates the need for compensation flights and complicated parameter extractions, integrating variations in flight attitudes into the UAV-borne vector MAG model for landmine detection.

In contrast to fluxgate vector magnetometer sensors, optically pumped sensors experience fewer attitude-related issues and mainly respond to their heading relative to the Earth's magnetic field. Magnetic maps or magnetic gradiometric maps are commonly used in geophysical exploration, such as shallow archaeological UAV-based surveys, because they can quickly cover large areas and detect soil disturbance anomalies [40–44]. These methods rely on highly sensitive total field magnetometers, such as cesium vapor magnetometers. However, due to their higher cost and greater complexity in payload configuration compared to simpler fluxgate vector magnetometers, further research is

needed to assess their practical use in specialized applications like UAV-based landmine detection, as discussed in this paper.

Our next research focus will be on enhancing detection capabilities for moving magnetic targets using our refined UAV-borne MAG model. This will involve further development and validation of our approach to ensure that it meets the demands of dynamic and complex flight environments.

5. Conclusions

This study successfully detected landmines at low altitudes using a simple vector magnetometer system mounted on a drone, avoiding the need for complex horizontal or vertical gradient systems and compensation procedures. Through simulations and experiments with our innovative UAV-borne vector MAG system, we accurately estimated the burial depth and magnetic moment of landmines. Our UAV-borne vector MAG model, which uses a magnetic dipole approach, introduced a novel data-processing method and provided valuable insights into various flight conditions, including attitude, speed, survey line intervals, and altitude. Validation at a Korean Army exercise site confirmed the effectiveness of our approach. This comprehensive methodology, which integrates experiments, simulations, and advanced data processing, has developed a crucial UAV-borne MAG model that advances UAV-based landmine detection technology.

Author Contributions: Conceptualization, methodology, software, validation, formal analysis, investigation, resources, data curation, visualization, project administration, funding acquisition, writing—original draft preparation, J.L.; writing—review and editing, supervision, H.L. All authors have read and agreed to the published version of the manuscript.

Funding: Junghan Lee was supported by LIG Nex1. This work was supported by the National Research Foundation of Korea (NRF) grant funded by the Korea government (MSIT) (2021R1F1A1057455).

Data Availability Statement: The raw data supporting the conclusions of this article will be made available by the authors on request.

Conflicts of Interest: Author Junghan Lee was employed by the company LIG Nex1 Co., Ltd. The other author declares that the research was conducted in the absence of any commercial or financial relationships that could be construed as a potential conflict of interest.

References

1. Schartel, M.; Burr, R.; Bähnemann, R.; Mayer, W.; Waldschmidt, C. An experimental study on airborne landmine detection using a circular synthetic aperture radar. *arXiv* **2020**, arXiv:2005.02600.
2. Grathwohl, A.; Arendt, B.; Grebner, T.; Waldschmidt, C. Detection of Objects Below Uneven Surfaces With a UAV-Based GPSAR. *IEEE Trans. Geosci. Remote Sens.* **2023**, *61*, 1–13. [[CrossRef](#)]
3. Yoo, L.-S.; Lee, J.-H.; Ko, S.-H.; Jung, S.-K.; Lee, S.-H.; Lee, Y.-K. A drone fitted with a magnetometer detects landmines. *IEEE Geosci. Remote Sens. Lett.* **2020**, *17*, 2035–2039. [[CrossRef](#)]
4. Yoo, L.-S.; Lee, J.-H.; Lee, Y.-K.; Jung, S.-K.; Choi, Y. Application of a drone magnetometer system to military mine detection in the demilitarized zone. *Sensors* **2021**, *21*, 3175. [[CrossRef](#)]
5. Romero, I.; Walter, T.; Mariager, S. Wavelet Transform Analysis for a Continuous Wave Metal Detector for UAV Applications. In Proceedings of the IGARSS 2023–2023 IEEE International Geoscience and Remote Sensing Symposium, Pasadena, CA, USA, 16–21 July 2023; pp. 4764–4767.
6. Romero, I.; Walter, T.; Mariager, S. Depth Analysis for Continuous Wave Metal Detector for UAV Applications. In Proceedings of the IGARSS 2023–2023 IEEE International Geoscience and Remote Sensing Symposium, Pasadena, CA, USA, 16–21 July 2023; pp. 4650–4653.
7. Lee, J.; Lee, H.; Ko, S.; Ji, D.; Hyeon, J. Modeling and Implementation of a Joint Airborne Ground Penetrating Radar and Magnetometer System for Landmine Detection. *Remote Sens.* **2023**, *15*, 3813. [[CrossRef](#)]
8. Kim, J.; Brown, M.A.; Head, B.; Defeat, E.H. Detection System (SoRIDS) Demonstration Quicklook. Available online: <https://apps.dtic.mil/sti/pdfs/AD1174381.pdf> (accessed on 8 June 2024).
9. Rullo, C.M.C.S.J. BALTOPS 50 Site For Experimental Mine Hunting Equipment. Available online: <https://www.c6f.navy.mil/Press-Room/News/News-Display/Article/2656044/bal tops-50-site-for-experimental-mine-hunting-equipment/> (accessed on 8 June 2024).

10. Wu, Y.; Huang, W. Studies and analysis on unintentional electromagnetic radiation of UAV. In Proceedings of the 2015 IEEE 6th International Symposium on Microwave, Antenna, Propagation, and EMC Technologies (MAPE), Shanghai, China, 28–30 October 2015; pp. 479–482.
11. Kim, S.; Noh, Y.-H.; Lee, J.; Lee, J.; Choi, J.-S.; Yook, J.-G. Electromagnetic signature of a quadcopter drone and its relationship with coupling mechanisms. *IEEE Access* **2019**, *7*, 174764–174773. [[CrossRef](#)]
12. Barrowes, B.E.; Glaser, D.R.; Quinn, B.G.; Prishvin, M.; Shubitidze, F.; RESEARCH, C.R.; States, E.L.H.N.H.U. *Unmanned Aerial Systems Electromagnetic Induction Sensor Development: Evaluation of Commercial-off-the-Shelf Unmanned Aerial System Motor Interference and Mitigation in Airborne Electromagnetic Induction Sensors*; US Army Engineer Research and Development Center, Cold Regions Research and Engineering Laboratory and Dartmouth College, Thayer School of Engineering: Hanover, NH, USA, 2019.
13. Parvar, K. Development and Evaluation of Unmanned Aerial Vehicle (UAV) Magnetometry Systems. Master’s Thesis, Queen’s University, Kingston, ON, Canada, 2016.
14. Tuck, L. Characterization and Compensation of Magnetic Interference Resulting from Unmanned Aircraft Systems. Ph.D. Thesis, Carleton University, Ottawa, ON, Canada, 2019.
15. Kan, X.; Thomas, J.; Teng, H.; Tanner, H.G.; Kumar, V.; Karydis, K. Analysis of ground effect for small-scale uavs in forward flight. *IEEE Robot. Autom. Lett.* **2019**, *4*, 3860–3867. [[CrossRef](#)]
16. Zheng, Y.; Li, S.; Xing, K.; Zhang, X. Unmanned aerial vehicles for magnetic surveys: A review on platform selection and interference suppression. *Drones* **2021**, *5*, 93. [[CrossRef](#)]
17. Wu, H.; Pei, X.; Li, J.; Gao, H.; Bai, Y. An improved magnetometer calibration and compensation method based on Levenberg–Marquardt algorithm for multi-rotor unmanned aerial vehicle. *Meas. Control* **2020**, *53*, 276–286. [[CrossRef](#)]
18. Spielvogel, A.R.; Whitcomb, L.L. A stable adaptive observer for hard-iron and soft-iron bias calibration and compensation for two-axis magnetometers: Theory and experimental evaluation. *IEEE Robot. Autom. Lett.* **2020**, *5*, 1295–1302. [[CrossRef](#)]
19. Calou, P.; Munschy, M. Airborne magnetic surveying with a drone and determination of the total magnetization of a dipole. *IEEE Trans. Magn.* **2020**, *56*, 1–9. [[CrossRef](#)]
20. Kaub, L.; Keller, G.; Bouligand, C.; Glen, J.M. Magnetic surveys with Unmanned Aerial Systems: Software for assessing and comparing the accuracy of different sensor systems, suspension designs and compensation methods. *Geochim. Geophys. Geosystems* **2021**, *22*, e2021GC009745. [[CrossRef](#)]
21. Munschy, M.; Boulanger, D.; Ulrich, P.; Bouiflane, M. Magnetic mapping for the detection and characterization of UXO: Use of multi-sensor fluxgate 3-axis magnetometers and methods of interpretation. *J. Appl. Geophys.* **2007**, *61*, 168–183. [[CrossRef](#)]
22. Mu, Y.; Chen, L.; Xiao, Y. Small Signal Magnetic Compensation Method for UAV-Borne Vector Magnetometer System. *IEEE Trans. Instrum. Meas.* **2023**, *72*, 1–7. [[CrossRef](#)]
23. Qiao, Z.; Zhou, S.; Jiao, J.; Yu, P.; Zhang, Z.; Zhou, W.; Wu, G. Research on aeromagnetic three-component error compensation technology for multi-rotor UAV. *J. Appl. Geophys.* **2021**, *193*, 104406. [[CrossRef](#)]
24. Kulüke, C.; Virgil, C.; Stoll, J.; Hördt, A. A new system to measure the gradient vector of the magnetic field on unmanned aerial vehicles—data processing and field experiment. *RAS Tech. Instrum.* **2022**, *1*, 65–80. [[CrossRef](#)]
25. SF11c from Lightware. Available online: <https://www.documents.lightware.co.za/SF11%20-%20Laser%20Altimeter%20Manual%20-%20Rev%2010.pdf> (accessed on 10 June 2024).
26. C-RTK 9Ps from CUAV. Available online: <https://doc.cuav.net/gps/c-rtk-series/en/c-rtk-9ps/#datasheet> (accessed on 10 June 2024).
27. 1540 Magnetometer From Applied Physics. Available online: https://appliedphysics.com/wp-content/uploads/2023/09/Model1540_DEF_DataSheet_vA.pdf (accessed on 8 August 2024).
28. Psiaki, M.L.; Martel, F.; Pal, P.K. Three-axis attitude determination via Kalman filtering of magnetometer data. *J. Guid. Control. Dyn.* **1990**, *13*, 506–514. [[CrossRef](#)]
29. Drăgășanu, C.; Stoica, A. Single Sensor 3-Axis Attitude Determination System for Cubesats. Available online: https://www.scientificbulletin.upb.ro/rev_docs_arhiva/full2e_868270.pdf (accessed on 11 June 2024).
30. Natanson, G.; Challa, M.; Deutschmann, J.; Baker, D. Magnetometer-only attitude and rate determination for a gyro-less spacecraft. In Proceedings of the Third International Symposium on Space Mission Operations and Ground Data Systems, Part 2, Greenbelt, MD, USA, 14–18 November 1994.
31. LattePanda 3 Delta from LattePanda. Available online: https://docs.lattepanda.com/content/3rd_delta_edition/specification/ (accessed on 10 June 2024).
32. MK15 from SIYI. Available online: https://siyi.biz/siyi_file/MK15/MK15%20User%20Manual%20v1.5.pdf (accessed on 10 June 2024).
33. pMDDL5824 Modem from Microhard. Available online: <https://www.microhardcorp.com/brochures/pMDDL5824.Brochure.Rev.1.2.0.pdf> (accessed on 10 June 2024).
34. Wang, J.; Jiang, Z.; Gao, J.; Zhao, S.; Zhai, W.; Shen, Y. Frequency characteristics analysis for magnetic anomaly detection. *IEEE Geosci. Remote Sens. Lett.* **2021**, *19*, 1–5. [[CrossRef](#)]
35. Florsch, N.; Camerlynck, C.; Kammenthaler, M.; Muhlach, F. *Everyday Applied Geophysics 2: Electromagnetics and Magnetics*; ISTE Press Limited-Elsevier Incorporated: London, UK, 2018.

36. Mu, Y.; Xie, W.; Zhang, X. The joint UAV-borne magnetic detection system and cart-mounted time domain electromagnetic system for UXO detection. *Remote Sens.* **2021**, *13*, 2343. [[CrossRef](#)]
37. Burger, H.R.; Burger, D.C.; Burger, H.R. *Exploration Geophysics of the Shallow Subsurface*; Prentice Hall: Hoboken, NJ, USA, 1992; Volume 8.
38. Operator's and Unit Maintenance Manual for Land Mines. Available online: <http://mines.duvernois.org/LandMines.pdf> (accessed on 31 July 2024).
39. IAGA V-MOD Geomagnetic Field Modeling: International Geomagnetic Reference Field IGRF-13. Available online: <https://www.ngdc.noaa.gov/IAGA/vmod/igrf.html> (accessed on 8 August 2024).
40. Florio, G.; Celli, F.; Speranza, L.; Castaldo, R.; Pierobon Benoit, R.; Palermo, R. Multiscale techniques for 3D imaging of magnetic data for archaeo-geophysical investigations in the Middle East: The case of Tell Barri (Syria). *Archaeol. Prospect.* **2019**, *26*, 379–395. [[CrossRef](#)]
41. Schmidt, V.; Becken, M.; Schmalzl, J. A UAV-borne magnetic survey for archaeological prospection of a Celtic burial site. *First Break.* **2020**, *38*, 61–66. [[CrossRef](#)]
42. Pisciotta, A.; Vitale, G.; Scudero, S.; Martorana, R.; Capizzi, P.; D'Alessandro, A. A lightweight prototype of a magnetometric system for unmanned aerial vehicles. *Sensors* **2021**, *21*, 4691. [[CrossRef](#)] [[PubMed](#)]
43. Stele, A.; Kaub, L.; Linck, R.; Schikorra, M.; Fassbinder, J.W. Drone-based magnetometer prospection for archaeology. *J. Archaeol. Sci.* **2023**, *158*, 105818. [[CrossRef](#)]
44. Accomando, F.; Florio, G. Drone-Borne Magnetic Gradiometry in Archaeological Applications. *Sensors* **2024**, *24*, 4270. [[CrossRef](#)] [[PubMed](#)]

Disclaimer/Publisher's Note: The statements, opinions and data contained in all publications are solely those of the individual author(s) and contributor(s) and not of MDPI and/or the editor(s). MDPI and/or the editor(s) disclaim responsibility for any injury to people or property resulting from any ideas, methods, instructions or products referred to in the content.